Accepted Manuscript

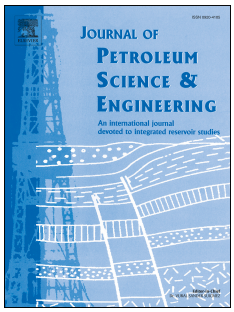

Systematic pore-scale study of low salinity recovery from Berea sandstone analyzed by micro-CT

Mehdi Shabaninejad, Jill Middlelton, Andrew Fogden

PII: S0920-4105(17)31029-X

DOI: 10.1016/j.petrol.2017.12.072

Reference: PETROL 4562

To appear in: *Journal of Petroleum Science and Engineering*

Received Date: 13 July 2017

Revised Date: 9 December 2017

Accepted Date: 22 December 2017

Please cite this article as: Shabaninejad, M., Middlelton, J., Fogden, A., Systematic pore-scale study of low salinity recovery from Berea sandstone analyzed by micro-CT, *Journal of Petroleum Science and Engineering* (2018), doi: 10.1016/j.petrol.2017.12.072.

Systematic pore-scale study of low salinity recovery from Berea sandstone analysed by micro-CT

Mehdi Shabaninejad[a], *Jill Middlelton*[a], *Andrew Fogden*[b]

[a] Department of Applied Mathematics, Research School of Physics and Engineering, Australian National University, Canberra, ACT 2601, Australia

[b] FEI Company, Suite 102, Level 1, 73 Northbourne Avenue Canberra, ACT 2600, Australia

Corresponding Author : Mehdi Shabaninejad, Email: mehdi.shabaninejad@anu.edu.au

ABSTRACT

The low salinity effect in clay-rich outcrop sandstones is probed by micro-CT imaging and analysis. A set of eight Berea sandstone mini-plugs underwent primary drainage and aging in crude oil to a mixed-wet state, followed by spontaneous imbibition of high and low salinity brines and imaging of this sequence of prepared starting and endpoint states. Tomogram registration and analysis were used to determine the salinity-induced changes in oil volume, oil/rock and oil/brine interfacial areas, and oil/brine interfacial mean curvature. Pore-scale statistics were extracted to explore any local correlation between the low salinity effect and pore geometry/topology. The qualitative observations and quantitative analyses demonstrated that the small oil recovery by the low salinity effect corresponded to a slight shift towards water-wet.

Keywords: Low salinity water flooding, Spontaneous imbibition, Micro CT, Image Analysis, wettability

1. Introduction

Laboratory and field data shows that oil recovery from clay-containing sandstones can increase by reduction of injected brine salinity. However the amount of incremental oil recovery by low salinity is very variable and difficult to predict, due to insufficient understanding of this process (Morrow and Buckley 2011, Masalmeh et al. 2014).

In recent years, many researchers have attempted to determine the mechanism(s) behind additional oil recovery by low salinity flooding, referred to as the low salinity effect. Early studies pointed out that an initial water saturation and clay, especially kaolinite, are necessary for the low salinity effect, and suggested that fines migration was likely responsible for displacing oil adhering to these fines (Tang and Morrow 1999). However, the low salinity effect was also observed in kaolinite-free rocks and in the absence of formation damage (Aladasani et al. 2012, Cissokho 2010). pH increase is often reported during low salinity water flooding and was considered as an alternative explanation for the low salinity effect (McGuire 2005). Other researchers proposed that multicomponent ion exchange (Lager et al. 2006) or double layer electrostatic repulsion (Ligthelm 2009) was responsible for the oil release. While it is widely accepted that oil/brine/rock interactions play a central role in the low salinity effect, the specific mechanism(s) remain debated (Yasaman Assefa et al. 2014). An osmotic pressure mechanism was also introduced recently, based on oil acting as a semipermeable membrane (for water but not ions), to provide the driving force to move oil droplets and open new pathways (Sandengen and Arntzen 2013). Organic acids can affect low salinity waterflooding performance. For example, absorption of amino acids to clay surfaces in salt free aqueous solutions is higher than high salinity solutions (Wang, and Lee 1993, Parfitt and Greenland 1970)

One of main complications in understanding the low salinity effect is unscrambling the difference between cause and effect in observed results. Some of the above-mentioned proposed mechanisms may only be a side effect rather than a root cause. Wettability shift toward water-wetting has been observed in most low salinity core flooding studies (Berg et al. 2010, Cense et al 2011, Rivet et al. 2010, Sorop et al. 2014), and results from a switch in oil/brine/rock electrostatic interactions to favor repulsion of oil from mineral across brine. In spontaneous imbibition experiments, these interactions between liquids and rock drive recovery without imposition of any external force. Spontaneous imbibition is thus a suitable mode, and perhaps a better operative condition compared to core flooding, to focus on rock wettability changes and their link to pore-scale displacements and the low salinity effect.

Micro-Ct studies of low salinity of sandstone reservoir shows that low salinity brine can redistribute oil configuration in well swept area without changing in oil recovery (Shabaninejad et al. 2015). In their later study effect of local mineralogy on low salinity responses was studied

using micro-CT and SEM-EDS tools and pointed out that oil release from external surface of minerals by low salinity brine was less favored from kaolinite (and from muscovite) than from silicate grains (Shabaninejad et al. 2017). Fast X-Ray micro-CT technique was also utilized to study oil configuration after high and low salinity and the results showed that low salinity brine changed the oil distribution in small pores of Berea sandstones (Bartels et al. 2017).

However, resolution of pore-scale details such as shapes of menisci generally requires that the micro-CT imaging be performed on small plugs, called mini-plugs. Further, an X-ray dense agent must be added to oil or brine to selectively increase its attenuation and so provide contrast between these two liquid phases. The challenge is thus to analyze the pore-scale changes of the low salinity effect without introducing artifacts or nullifying the effect due to these imaging requirements and related perturbations, including effects of X-ray exposure and heightened sensitivity to rock damage, air bubbles and other contaminants.

2. Materials and Methods

Three Berea outcrop sandstone samples labeled A, B and C were used in this study. Samples A and B had air permeability of ~ 60 mD and porosity of 18.3% and 17.9%, respectively, from MICP, while sample C had air permeability of ~ 500 mD and porosity of 19.5% from MICP. The crude oil used was from the Minnelusa formation, with density and viscosity of 0.9062 gcm^{-3} and 77.2 mPa.s at 20 °C. It has n-C_7 asphaltene content of 9.0 wt % and acid and base numbers of 0.17 and 2.29 mg KOH/g oil, respectively. The initial (connate) and high salinity brine corresponded to Minnelusa reservoir brine (MRB), while the tested low salinity brines were 20- or 100-fold dilutions of the high salinity brine (0.05MRB or 0.01MRB). The rock, oil and brine thus match those used in the plug-scale study of the low salinity effect by the group of Morrow (Zhang and Morrow 2006). For micro-CT imaging, the Berea samples were cored to 3 or 5 mm diameter mini-plugs using a manually-fed drill press with air as lubricant, and then cut using a diamond-blade saw to a length of 12.5 mm. Further, X-ray attenuation contrast was introduced via a so-called contrast brine, prepared by substituting 0.3 M NaCl for 0.3 M NaI (sodium iodide) in the high salinity brine recipe. The compositions of the MRB and Contrast brine are given in Table 1. All brines were vacuum degassed and adjusted with NaOH or HCl to pH 6.1-6.3 prior to use to have fair comparison of high and low salinity brine and avoid any pH effect on oil recovery (McGuire et al., 2005)

Table 1. Minnelusa Reservoir brine and Contrast brine compositions.

Brine	NaCl mmol/l	$CaCl_2.2H_2O$ mmol/l	$MgCl_2.6H_2O$ mmol/l	Na_2SO_4 mmol/l	NaI mmol/l	IS mmol/l	TDS g/l
Minnelusa RB	496.0	19.0	7.0	48.6	0	719.5	38.6
Contrast Brine	196.0	19.0	7.0	48.6	300.0	719.5	66.09

The rock samples were additionally characterized for spatial mineralogy and pore throat radius. For mineralogy, sister mini-plugs of 5 mm diameter were embedded in epoxy resin, cut crosswise or lengthwise and polished. 2D mineral maps of these polished sections were generated using automated SEM-EDS acquisition and analysis by QEMSCAN (FEI) acquired at 3 µm step size (See the Supplementary material). Figure 1(a-c) presents corresponding distributions of each of these three Berea samples. Strong similarities between the three are evident, although sample A possesses less quartz, compensated by more of most of the other minerals. Of the average of 4.5% clay present per sample, the main clay mineral is kaolinite, although muscovite/illite, biotite and chlorite also occur in significant fractions. The MICP curves in Figure 1(d) show that samples A and B are very similar, while C has somewhat larger pore throats, as expected from its higher permeability.

Each mini-plug was mounted in its sealed aluminum-tube holder for scanning, first in its dry state and then after oil recovery by spontaneous imbibition of high and low salinity brine, and in some cases again after imbibition of even lower salinity brine. Most mini-plugs were scanned over their middle section using a standard circular trajectory, although one mini-plug was scanned over a greater height and at higher fidelity using a helical trajectory on a HeliScan instrument.

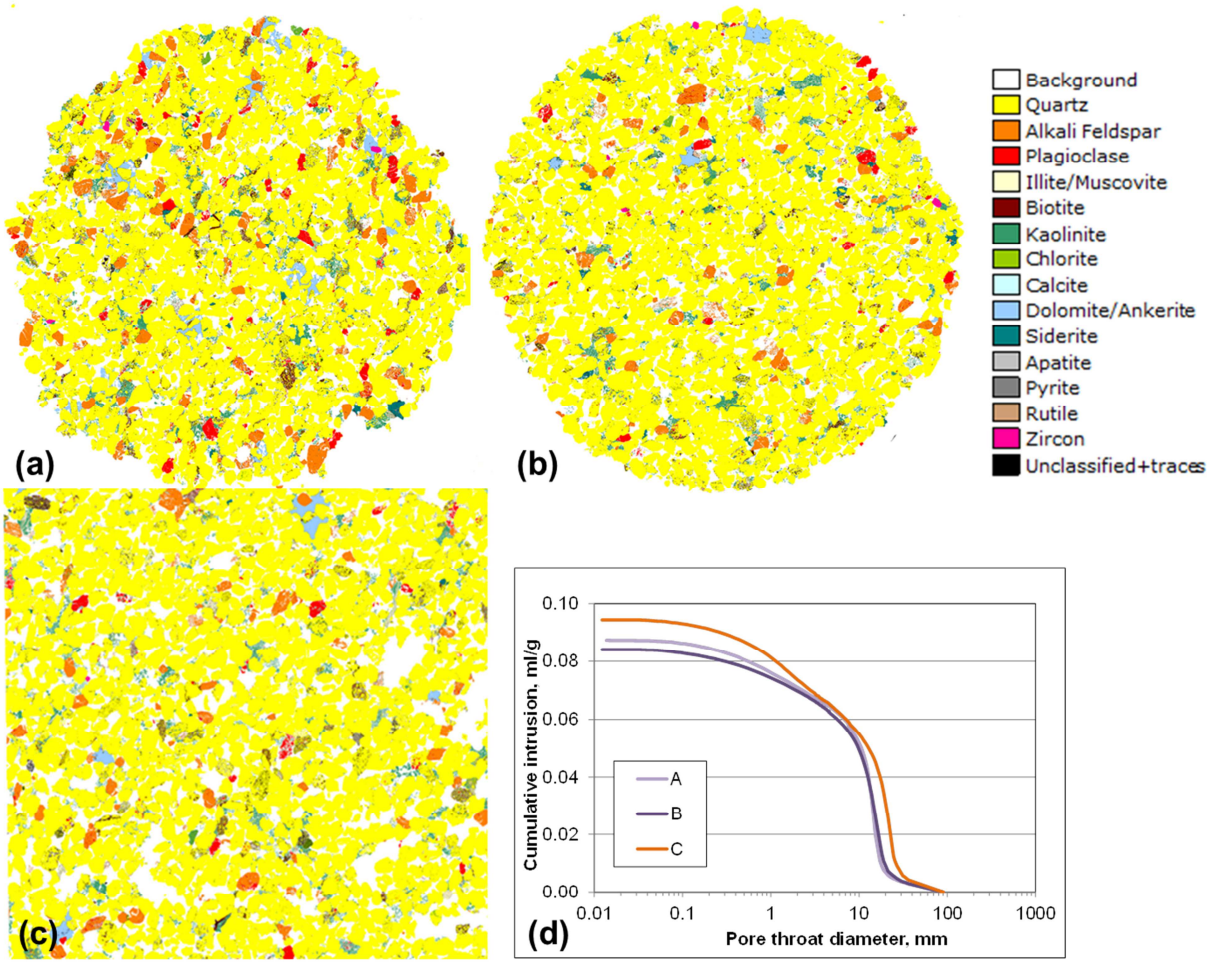

Figure 1 Mineral maps from QEMSCAN of mini-plug sections of Berea sandstone samples (a) A, (b) B, and (c) C; (d) Cumulative mercury intrusions for all three Berea samples.

After micro-CT scanning in its dry state, each mini-plug was saturated with Minnelusa reservoir brine (MRB) by evacuation and vacuum infiltration for 3-4 hours. It was then transferred to a glass vial filled with crude oil and with 1 g of sand bed at the bottom. The mini-plug in its vial was centrifuged at the chosen speed (capillary pressure) for 20 min in each direction to uniformize the irreducible brine saturation profile. The mini-plug was then transferred to a second glass vial prefilled with crude oil and with its lid sealed by epoxy, and aged in an oven at 75 °C for 14 days. The first vial, with its oil and sand bed containing the drained brine, was used to measure the average initial water saturation of the mini-plug from the difference in brine mass between that originally saturating the mini-plug and that drained during centrifugation. The former was determined gravimetrically from the weight difference between the brine-saturated

and dry state of the mini-plug. The latter was inferred from titration, by pipetting off the oil above the sand bed and homogenizing the remaining oil and brine in the sand by adding 1.9 g of dichloromethane (DCM) and 0.7 g of methanol, from which the blend's water content was determined by Karl Fischer titration.

Spontaneous imbibition (SI) was performed by transferring the aged plug to a vial containing 2.5 ml of brine (usually MRB) for secondary recovery at 75 °C for 7 days. Following this high salinity recovery step, the plug was transferred to another vial containing 2.5 ml of Contrast brine (see Table 1) at room temperature for 3 days, to allow diffusional exchange of MRB for Contrast brine (i.e. diffusion of Cl^- out and I^- in). This exchange step, to heighten the X-ray attenuation of the brine phase above that of oil, was conducted at room temperature to prevent or minimize any extraneous oil production or movement. The immersed mini-plug in contrast brine was micro CT scanned after first spontaneous imbibition. The scanned mini-plug was then transferred back to a vial containing 2.5 ml of the un-doped brine (usually MRB) at room temperature for 3 days to allow diffusional re-exchange of Contrast brine for un-doped brine. A second spontaneous imbibition was then performed by immersing the mini-plug in 2.5 ml of a second brine (usually diluted MRB) at 75 °C for 7 days. After this low salinity recovery step in tertiary mode, the above-mentioned transfer to Contrast brine was repeated for imaging of this second imbibed and exchanged state. Care was taken during all steps to avoid air entering the pore space, i.e. always all brines were degassed before immersing mini-plugs and also mini-plug was transformed to the vials under the brine.

The 3D tomograms of each mini-plug in its dry state and after spontaneous imbibition of high salinity brine (SIH) and in turn low salinity brine (SIL) or very low salinity brine (SILL) were reconstructed and then post-processed and analyzed using Mango software. After masking to exclude the plug holder walls, the tomograms of the spontaneously imbibed states were registered into perfect alignment with the dry-state tomogram. Segmentation was then performed using a converging active contours algorithm (Sheppard et al, 2004) to distinguish the oil and brine phases for calculation of residual oil saturation and metrics of its distribution.

3. Results and Discussion

3.1 Tomogram observation and Image analysis of residual oil

Table 2 lists all experiments performed on the eight samples and their key details and results. Each row corresponds to an imaged state, the naming of which in the first column follows the formula: mini-plug number (1-8), Berea sample (A-C), imbibition experiment number (1-3), and imbibing brine (H = MRB, L = 0.05MRB, LL = 0.01MRB). For example, the state in the first row **1_A_1_H** is the first mini-plug studied, taken from Berea sample A, imaged after its first spontaneous imbibition (secondary recovery), of high salinity brine MRB.

Columns 2-6 of Table 2 list the experimental details, namely the mini-plug diameter, the porosity from MICP on the sister sample of Berea A-C from Figure 1(d), the centrifuge spin speed used in primary drainage, the initial brine saturation determined from gravimetric and titration measurements as described above, and the brine used in subsequent spontaneous imbibition. Columns 7-9 list the results from segmentation of residual oil in the tomogram corresponding to this imbibition step (SIH, SIL or SILL). In particular, two-phase segmentation of each such imaged state was performed to distinguish the residual oil resolved at the tomogram voxel size of approximately 2 or 3 μm for the 3 or 5 mm diameter mini-plugs, respectively. Figure 2 displays an example of the result of this segmentation. The remainder of space comprises the grains and clays and brine occupying the rest of the resolved pores (referred to as macro-pores) and filling the sub-resolution microporosity. Instances of oil in micro-pores were comparatively rare and were not considered in this simplest segmentation, but will be analyzed in the next sub-section.

Table 2 Experimental details of Berea mini-plugs and residual oil segmentation results.

Sample Name	Diameter (mm)	Φ (MICP) (%)	Spin speed (rpm)	Swi (%PV)	Flood Brine	Sor (%PV)	RF (%OOIP)	ΔRF (%OOIP)
1_A_1_H	3	18.3	2250	36.0	MRB	49.0	23.4	
1_A_2_L	3	18.3	2250	36.0	0.05MR	43.4	32.3	8.9
2_A_1_H	3	18.3	3500	9.3	MRB	38.9	57.1	
2_A_2_LL	3	18.3	3500	9.3	0.01MR	38.2	57.9	0.8
3_A_1_L	3	18.3	3500	6.6	0.05MR	38.4	58.9	
3_A_2_LL	3	18.3	3500	6.6	0.01MR	37.8	59.6	0.7
4_B_1_H	3	17.9	3500	12.4	MRB	39.4	55.0	

5_B_1_L	3	17.9	3500	16.3	0.05MR	38.8	53.6	
6_C_1_H	3	19.5	2250	39.1	MRB	28.9	52.5	
7_C_1_H	5	19.5	3000	18.2	MRB	54.6	33.3	
7_C_2_L	5	19.5	3000	18.2	0.05MR	52.1	36.3	3.0
8_C_1_L	5	19.5	3000	18.2	0.05MR	54.5	33.4	
8_C_2_H	5	19.5	3000	18.2	MRB	54.1	33.8	0.4
8_C_3_LL	5	19.5	3000	18.2	0.01MR	52.7	35.6	1.8

Column 7 lists average residual oil saturation which was calculated by division of volume fraction of segmented residual oil by MICP porosity in column 3. Oil recovery factor *RF* was calculated as a percentage of original oil in place (OOIP) in column 9 as:

$$RF(\%OOIP) = \frac{S_{oi} - S_{or}}{S_{oi}} \times 100 \qquad (1)$$

where S_{oi} =1-S_{wi} is initial oil saturation from column 5 and S_{or}(%PV) is from column 7. Enhanced oil recovery, Δ*RF*, shown in the last column of Table 2, is the increment in *RF* from one state of spontaneous imbibition (e.g. SIH) to the next (e.g. SIL).

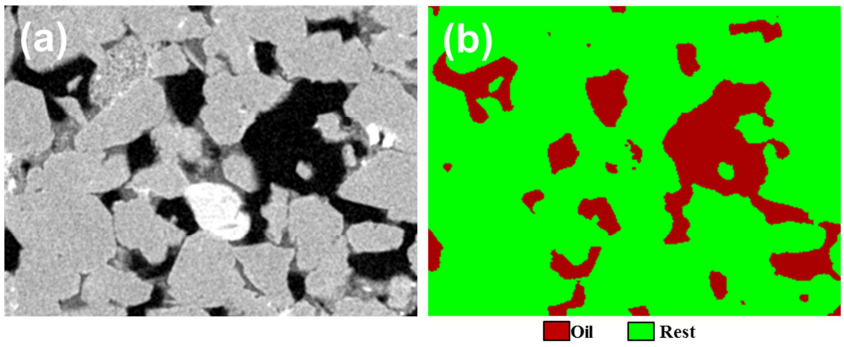

Figure 2. Tomogram subarea (1.1 mm × 0.8 mm) of sample 7_C after (a) SIH and (b) its two-phase segmentation into oil and the remainder.

The first two mini-plugs studied, 1_A and 6_C, were primary drained to relatively low capillary pressure, yielding very high Swi (36.0% and 39.1%, respectively). Centrifuge spin speed was increased to achieve lower S_{wi} in the subsequent six mini-plugs. The 3 mm diameter mini-plugs of Berea A remained intact through the planned pair of imaged states of spontaneous imbibition in Table 2. Those of Berea B and C broke on handling after their first imaged state, so no

evaluation of incremental recovery in tertiary mode was possible. Owing to their delicacy, and to the higher permeability of Berea C, later experiments on this sample used mini-plugs (7_C and 8_C) of 5 mm diameter, which remained intact through their planned imaging sequences.

The Contrast brine used for exchange after the first spontaneous imbibition of the first mini-plug tested (state 1_A_1_H) contained 0.15 M NaI rather than the 0.3 M NaI in Table 1. This low concentration of dopant was used to minimize perturbation of the imbibed state during the ion exchange step. However, the resulting X-ray attenuation contrast between oil and brine was so weak that segmentation of oil in the tomogram became difficult and ambiguous. The concentration of NaI in the Contrast brine was thus increased to 0.3 M in all subsequent imaged states. Figure 3 shows a zoom-in sub region of the tomogram sequence of mini-plug 1_A registered between its dry state and after SIH and after SIL.

The incremental recovery factor of 8.9% due to low salinity in this first mini-plug 1_A in Table 2 is much greater than in all other subsequently tested mini-plugs. In Figure 3, the distribution and shape of residual oil after SIH is suggestive of a mixed-wet state. Oil recovery by low salinity brine, via release from surfaces of grains and clay aggregates bounding larger pores, appears to be substantial. On the other hand, oil in smaller pores between pore-filing kaolinite booklets (near the top in Figure 3) does not appear to have been displaced. Some local movement of fines also occurs in association with the additional oil displacement. The high incremental recovery may stem in part from the low secondary recovery factor (lowest of all mini-plugs) and in part from the above-mentioned uncertainty in oil segmentation of the SIH tomogram, and thus the results for mini-plug 1_A in Table 2 should best be regarded as an outlier.

Mini-plug 2_A (See Supplementary material) underwent SIH in secondary mode and SILL in tertiary mode. Compared to 1_A, this mini-plug was drained to lower Swi (9.3%), and yet the resolved oil blob shapes after SIH are now more suggestive of a weakly water-wet state with relatively small brine-advancing contact angles. Occurrence of oil within kaolinite aggregates is also rarer than in 1_A. These observations are consistent with the much higher recovery factor (57.1%) by spontaneous imbibition. Incremental recovery from 2_A by (very-) low salinity brine was the least of all mini-plugs in Table 2, possibly owing to this water-wet state after SIH allowing little scope for extra recovery in SILL by further shift to more water-wet. The differences between mini-plugs 1_A and 2_A emphasize the variability in experiments on such

small sub-samples. The large matrix in Table 2 was thus tested to reduce this variability and obtain clearer overall indications of the low salinity effect.

Mini-plug 3_A (See Supplementary material) was drained down to an initial brine saturation of 6.6%, similar to 2_A, but then underwent SIL (rather than SIH) in secondary recovery mode, followed by SILL in tertiary mode. Residual oil saturation and recovery factor of SIL and SILL for 3_A were very similar to the corresponding values of SIH and SIL for 2_A. This implies that the low salinity effect is largely absent in both secondary and tertiary mode. The distribution of residual oil is qualitatively similar to that in 2_A and is consistent with a weakly water-wet state in which the adhesion of oil to rock only appears to be strong in certain locations. The switch from SIL to SILL results in occasional detachment of oil and withdrawal of the terminal meniscus, but usually to an insufficient extent to lead to overall recovery.

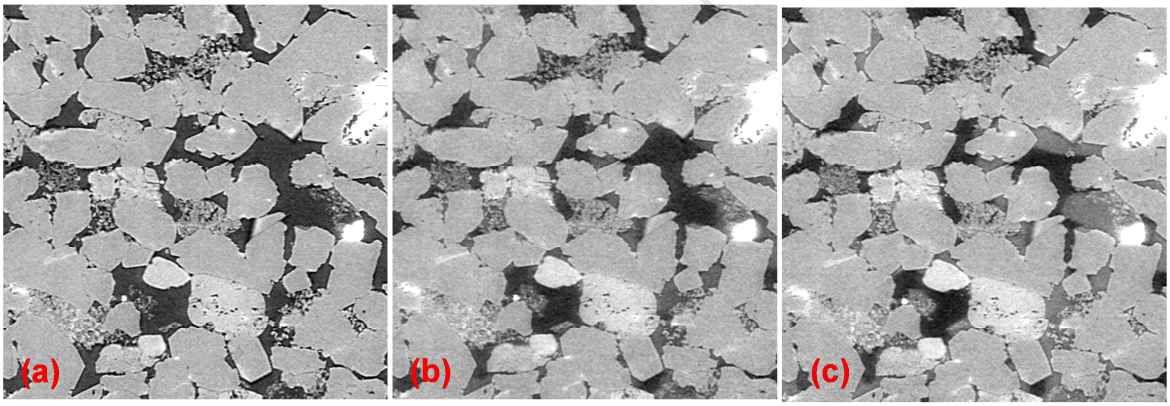

Figure 3 Zoom-in of a sub area of 1.0 mm × 1.1 mm of mini-plug 1_A registered between the (a) dry state, and the states after (b) SIH followed by (c) SIL.

Formation of water emulsions in the oil bulk during low salinity water flooding has been reported in several studies (Sandengen et al. 2013, Emadi and Sohrabi 2012) and has been hypothesized as an additional mechanism for oil recovery. Stable droplets of brine in oil were also observed in the Berea A mini-plugs of this study, with the highest amount in 1_A, occasional occurrence in 3_A, and only very rare instances in 2_A. Figure 4(a-d) shows registered subareas from 1_A and 3_A after their sequence of two imbibition states. Cyan circles show examples of oil displacement by detachment and meniscus movement, as described above,

during SIL in tertiary mode in 1_A. On the other hand, green circles show emulsified brine droplets that form during tertiary mode imbibition (SIL for 1_A and less commonly for SILL in 3_A).

These stable droplets generally form within larger pores that are completely oil-filled and that lie near the mini-plug periphery. The mechanism for their formation and stabilization is not fully understood. One possible explanation is that they form due to shearing of the oil during insertion of the mini-plug into its holder for imaging; however this would not seem to explain their preference for the SIL state. Another explanation is that they form by osmosic pressure, which acts to pump water molecules from the surrounding low salinity brine through the semi-permeable membrane of oil to hydrate pockets of high-salinity connate brine that have been disconnected and isolated by the pore-filling oil. In this case the hydration driving force that swells these locally isolated connate pockets to droplets must also reconnect them, since subsequent ion exchange of Cl^- for I^- in the Contrast brine (which cannot pass through oil) accesses and brightens the droplets in the tomogram.

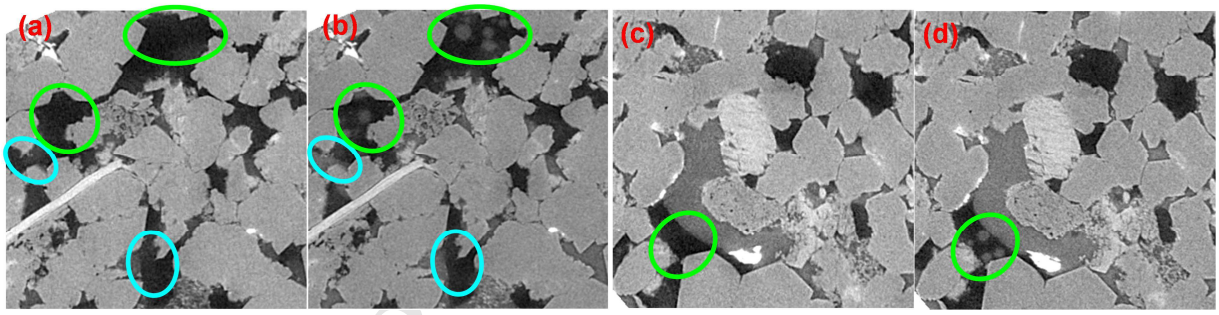

Figure 4. Subarea (0.66 mm × 0.66 mm) of tomogram cross-sectional slice of mini-plug 1_A, and registered between (a) SIH and (b) SIL, and similarly for mini-plug 3_A of the same sized subarea for (c) SIL and (d) SILL. Circles show low salinity brine displacing oil (cyan) and emulsified brine (green).

For the two mini-plugs 4_B and 5_B of 3 mm diameter cored from Berea B, in which only one state of spontaneous imbibition was imaged in Table 2, the results are qualitatively similar to those for 2_A and 3_A. The measured initial brine saturation is again fairly low and secondary recovery factor from segmentation of either SIH or SIL is around 55%, so no low salinity effect is apparent. Representative sub area of their tomograms, registered between the dry and imbibed states, are given in Figure 5 and Supplementary material. The oil distributions are suggestive of a

weakly water-wet or weakly mixed-wet state, in which partial recovery is associated with some local snap-off in water-wet locations, while the residual oil remains adhered to or pinned at locally more oil-wet locations on grains and on the extremities of pore-filling clay aggregates.

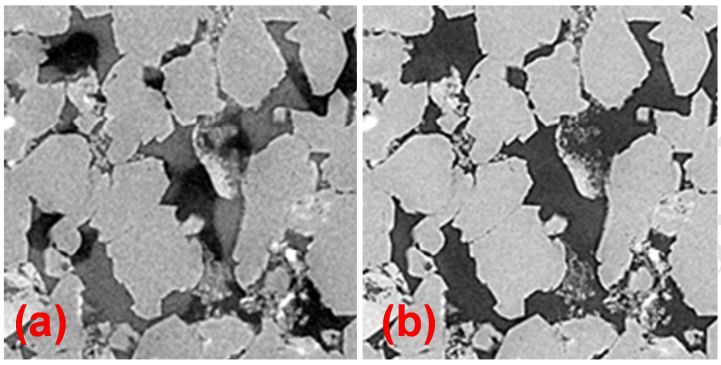

Figure 5. Subarea (0.66 mm × 0.66 mm) of tomogram cross-sectional slice of mini-plug 4_B, and registered between (a) dry and (b) SIH states.

Mini-plug 6_C was drained at low capillary pressure, resulting in high initial water saturation of 39.1% similar to 1_A. However its secondary recovery factor for SIH was much higher than for 1_A and almost as high as for mini-plugs 2-5, further suggesting that the disparate results for 1_A are an outlier. The residual oil distribution is again suggestive of a weakly mixed-wet state, in which recovery and snap-off from water-wet locations has occurred, while in other locations the oil blobs remain anchored to hinder further recovery. These anchoring sites often correspond to pore-filling clay, presumably kaolinite. Substantial mobilization of fines has taken place between the dry and SIH states (See Supplementary material). Some of these fines may have been created or liberated in the coring process and migrated further inwards, aided by the high permeability. This provided an additional reason for the switch from 3 to 5 mm diameter mini-plugs for the remainder of the Berea C studies.

For these subsequent two 5 mm diameter mini-plugs 7_C and 8_C in Table 2, primary drainage spin speed was increased to 3000 rpm, yielding a lower S_{wi} of 18.2%. These two mini-plugs of the more permeable Berea consistently gave higher S_{or} and lower recovery factor (in all modes) than the tighter mini-plugs 2-5. The imaging of mini-plug 7_C in its dry, secondary SIH and tertiary SIL states was performed using a helical trajectory on a HeliScan micro-CT scanner to

image a greater height (of the middle section) and at higher fidelity than for the circular scans of all other mini-plugs. A subarea of these three registered tomograms are shown in Figure 6. Most of the residual oil after SIH lies in the larger pores, while the smaller pores are mainly occupied by brine, and presumably were so throughout the restoration process. Again the overall impression is that the wettability state after SIH is weakly mixed-wet, with many menisci possessing low contact angles at their contacts with grains, while in other locations the oil lines the pore walls with high contact angle, or appears to be pinned to exhibit an intermediate angle.

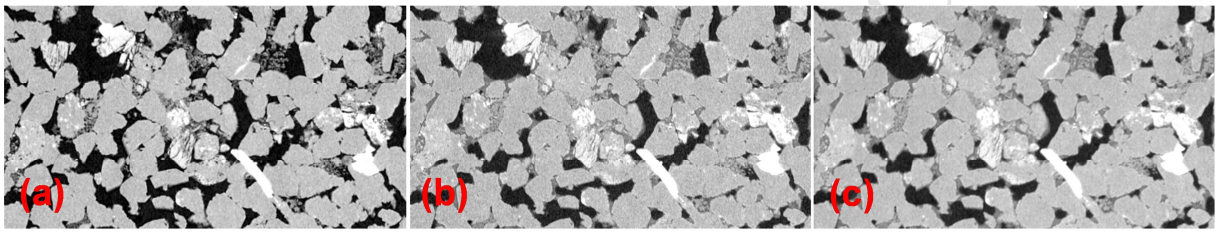

Figure 6. Sub area of 2.2 mm × 1.2 of mini-plug 7_C,registered between the (a) dry state, and the states after (b) SIH followed by (c) SIL.

Mini-plug 7_C exhibits a small but significant incremental recovery of 3.0% OOIP during subsequent SIL. From Figure 6, the extra recovery is mainly due to detachment of pinned oil from some contact points in intermediate-large pores, leading either to release and withdrawal of the existing oil meniscus or to a snap-off event. Oil blobs for which the meniscus spanning neighboring grains recedes slightly during SIL may be directly driven by brine advance at these sites, or by detachment at another site which indirectly causes this meniscus movement. The impression is that wettability shifts somewhat towards water-wet, although the majority of the oil is too strongly adhering or pinned to be mobilized in SIL. This mini-plug will be the subject of further analysis in the next sub-section.

To investigate other combinations of high and low salinity imbibition, mini-plug 8_C in Table 2 underwent the sequence SIL followed by SIH followed by SILL. From oil segmentation, the secondary recovery by SIL was virtually identical to that by SIH in 7_C, suggesting that no low salinity effect is operative in secondary mode. Further, the lack of additional recovery in 8_C from SIL to SIH served to demonstrate that the sequence of experimental steps before and after immersion in the brine of interest, involving exchange with Contrast brine and mini-plug

mounting and demounting, have little or no effect on oil recovery. The final change from SIH to SILL resulted in additional recovery from 8_C of 1.8% OOIP, which is less than that in 7_C but more than from the preceding (salinity increasing) step for 8_C. The oil distribution in this sample is qualitatively similar to that for 7_C, with most oil again found in larger pores while smaller pores between grains and even smaller ones within pore-filling clay aggregates remain brine-filled. The switch from SIL to SIH results in practically no pore-scale movement of oil, while the subsequent switch to SILL leads to some oil detachment and meniscus movement as for SIL in 7_C, although to a lesser extent.

3.2 Additional Classification of Oil Occupancy and Changes

Further image analysis in the current sub-section aims to apply more advanced techniques to extract more sensitive pore-scale measures of these slight changes. This is performed on mini-plug 7_C, since its tomograms have the largest field of view and highest quality, and its additional recovery of 3.0% OOIP by low salinity is intermediate to the extremes of large and very small tertiary recovery from mini-plugs 1-8. For this purpose, a segmentation workflow was developed to include contributions from sub-resolution microporosity, such as in clay aggregates.

Based on the history of oil/brine occupancy and the oil movement from secondary SIH to tertiary SIL, such as in mini-plug 7_C, voxels in the resolved pore space (referred to as macro-pores) fall into one of the following four possible categories of occupancy (Cheng 2015):

-BB (macro-pore voxels which remain brine filled in the SIH and SIL states)

-OO (macro-pore voxels which remain oil filled in the SIH and SIL states)

-OB (macro-pore voxels which were oil filled in the SIH state but became brine filled in the SIL state, i.e. where oil is displaced by low salinity brine)

-BO (macro-pore voxels which were brine filled in the SIH state but became oil filled in the SIL state, i.e. where oil displaced by low salinity brine re-invades a brine-occupied pore).

Sub-resolution porosity (referred to as micro-porosity), which is mainly hosted by pore-filling clay, is simply subdivided into the two complementary categories of:

-Micro-brine (micro-pore voxels occupied by brine)

-Micro-oil (micro-pore voxels occupied by oil).

Figure 7 shows a subarea of the registered tomogram series of mini-plug 7_C to illustrate with colored arrows examples of the macro- and micro-pore occupancy categories. The BB (blue) arrows indicate typical small resolved pores (dark in the dry tomogram) which are filled with brine in SIH and remain so after SIL. The OO (black) arrows show typical larger resolved pores that retain oil after both SIH and SIL processes. The OB (cyan) arrows show parts of resolved pores where residual oil after SIH was displaced by brine after SIL. One example of the rarest category of BO is shown by a red arrow, pointing to a small resolved pore (bounded by quartz grains and a weathered grain or pore-filling clay aggregate) which is filled with brine after SIH but is invaded by displaced oil after SIL.

Micro-porous clay aggregates can be filled with brine or oil or a coexisting combination of both. The purple arrow in Figure 7 shows an example of the micro-brine category, in the form of a pore-filling microporous clay aggregate which is brine filled after SIH and SIL (and presumably was so throughout the restoration process). The olive arrow shows a clay aggregate which contains micro-brine and micro-oil (in both SIH and SIL). Note that the distinction between macro-oil and micro-oil is arbitrarily set by tomogram resolution; some of the small oil droplets in this clay aggregate are almost resolvable, while others fall below this limit and constitute true micro-oil.

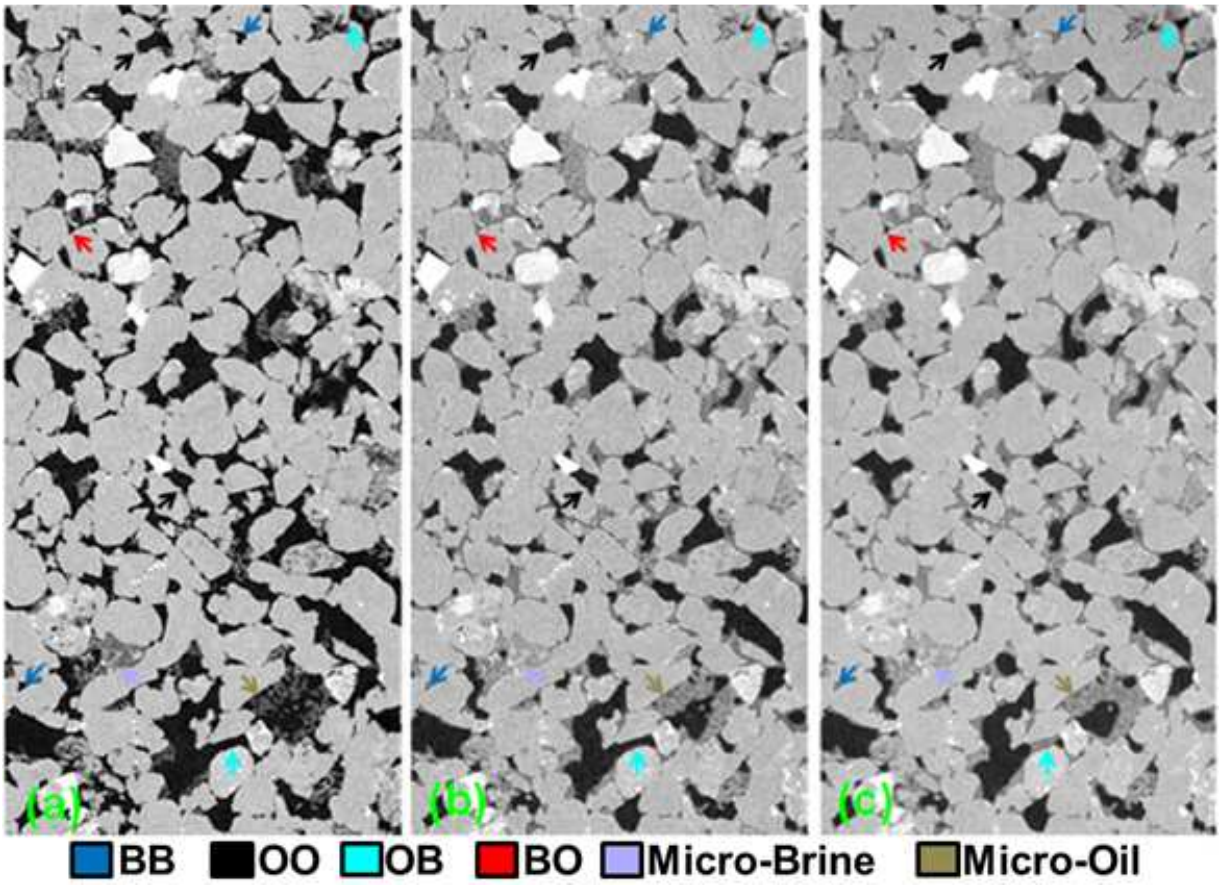

Figure 7. Subarea (4.9 mm × 2.4 mm) of tomogram longitudinal slice of mini-plug 7_C, registered between the (a) dry state, and the states after (b) SIH followed by (c) SIL, showing the definitions of pore occupancy classes.

3.3 Segmentation Workflow for Residual Oil

The primary segmentation (Figure 2) only addressed oil in resolved pores in the mini-plug tomograms, and the estimation of oil saturation relied upon MICP for the value of total porosity. The extension of this simplest treatment to segmentation of total porosity and oil in sub-resolution micro-pores requires the acquisition and registration of one additional tomogram (here of the mini-plug 7_C), namely in its state after saturation with the Contrast brine. This tomogram was acquired after all imbibition steps and subsequent solvent cleaning, followed by re-saturation of the mini-plug.

Figure 8 shows a subarea of the registered tomograms for this sequence of states: (a) dry, (b) brine saturated, (c) after SIH, and (d) after SIL. From these, the following difference tomograms were calculated (by subtracting the normalized attenuation grayscale value of corresponding voxels): (e) brine-saturated minus dry, (f) SIH minus dry, (g) brine-saturated minus SIH, and (h) SIL minus SIH. These difference maps were then used to assist in segmenting the various components of interest within the mini-plug, shown by the colors in Figure 8(i-l) as explained in the following paragraphs.

The dry tomogram in (a) suffices to segment the three phases in (i), referred to there as Grain (solid mineral), Pore Space (macro-pores) and Clay (including its micro-pores). The difference tomogram in (e) cancels out all contributions from the solid fraction of minerals (which thus become dark) to leave only the signal from macro-pores (bright) and micro-pores (intermediate grayscales). In particular, segmentation of (e) then quantifies the micro-porosity value at each voxel within the Clay phase as a linear function of the intermediate grayscale value there, shown in (j) (Sheppard et al 2014).

In this way the total macro-pore space and micro-pore space are identified, and thus once the fraction of these occupied by oil is determined, the remainder of each is the brine-occupied fraction. The resolved macro-oil after SIH (referred to as Oil in Figure 8) can be segmented directly from the SIH tomogram in (c) as the darkest phase, as was shown in Figure 2, or with greater sensitivity and consistency from the difference in (g) as the brightest phase. The difference in (f) or (g) within the Clay phase is then use to subdivide this intermediate phase into Brine-filled clay clusters (darker in (g)) and Oil-filled clay clusters (brighter in (g)). Figure 8(k) shows the resulting full subdivision of pore space into these four phases. The sub-resolution micro-oil after SIH is then obtained by applying the above-mentioned grayscale map of micro-porosity to the Oil-filled clay phase. The same procedure was also implemented for the corresponding tomogram and differences of the SIL state. The further categorization of resolved Oil and Brine phases into their four categories of occupancy history (BB, OO, OB and BO) is obtained from superposition of these segmentations of macro-oil and macro-brine in SIH and SIL. Alternatively, the tomogram difference between these two imbibed states in (h) can be used to identify OB and BO as the brightest and darkest phases (shown by cyan and red arrows, respectively), with the result given in (l).

The SIH tomogram is thus segmented into the five phases: grain, macro-oil, macro-brine, micro-oil and micro-brine. The SIL tomogram is segmented in the same way, and the resolved oil and brine phases can be further subdivided into the four pore occupancy categories (BB, OO, OB and BO). Note that macro-oil and macro-brine in SIL are OO + BO and BB + OB, respectively, while macro-oil and macro-brine in SIH are OO + OB and BB + BO, respectively.

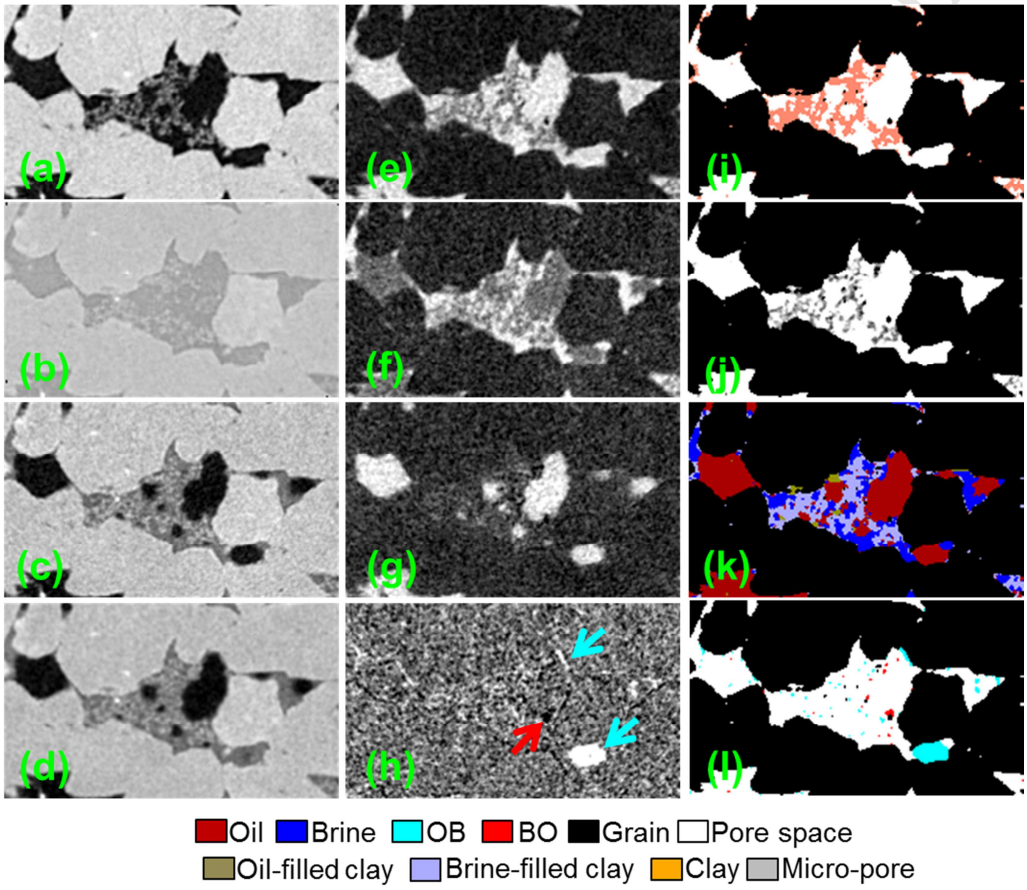

Figure 8. Subarea (0.7 mm × 0.4 mm) of tomogram cross-sectional slice of mini-plug 7_C, registered between the states: (a) dry, (b) brine saturated, (c) SIH, and (d) SIL, and the resulting differences: (e) brine-saturated minus dry, (f) SIH minus dry, (g) brine-saturated minus SIH, and (h) SIL minus SIH, leading to the segmentations of all components in (i)-(l).

Table 3 lists the volume fractions of these segmented phases, averaged over the entire masked tomogram of mini-plug 7_C. The porosity segmentation gives macro- and micro-porosity of 17.2% and 3.9%, respectively, for this tomogram voxel size cut-off of 3 µm. The total of 21.1%

is in reasonable agreement with the MICP value of 19.5% from sister material of Berea C. The resolved (macro-) oil fraction of this total pore volume is 57.8% and 54.1% in SIH and SIL, respectively. The discrepancy compared to the previous corresponding (macro-) estimates for S_{or} of 54.6% and 52.1%, respectively, in Table 2 is due to the differences in segmentation workflow (discussed further below) and in the segmented versus MICP porosity value used. The total (macro- plus micro-) oil recovery factor from Table 3 is 25.9 and 30.1%OOIP, respectively, giving an EOR increment from SIH to SIL of 4.1%OOIP, compared to 3.0%OOIP estimated in Table 2.

The subdivision into macro- and micro-pores in Table 3 clearly shows that residual oil is strongly biased to residing in macro-pores, occupying 71% after SIH and 67% after SIL of total available macro-pore volume. The corresponding fractions for oil in micro-pores after SIH and SIL are only 15% and 17%, respectively, of micro-pore capacity, as expected from the tendency for tight pores to remain brine-filled throughout restoration. The low salinity effect is thus only operative in macro-pores; in fact oil occupancy of micro-pores slightly increases from SIH to SIL (although the difference lies within segmentation uncertainty). This implies that if the low salinity effect involves oil release from clays, it can only occur from the external surfaces of clay aggregates (not within them) bounding macro-pores in this sample. The subdivision of macro-pores into their four categories of occupancy in SIH and SIL in the bottom row of Table 3 shows that the volume of oil re-displacing brine (BO) in SIL is very small relative to the reverse (OB).

Regarding the discrepancies and small inconsistencies between the two methods of segmentation, the direct, single-segmentation approach for macro-oil in is naturally limited by its neglect of micro-oil and its assumption that total porosity is represented by its MICP value. The use in the current Section of the extra tomogram of the brine-saturated state, together with registration for segmentations from multiple combinations of tomogram differences, reveals far more detailed and in-depth information, although these details and high-order measures are understandably more sensitive to artifacts and accumulated errors. The main sources of segmentation error, aside from operator subjectivity in choice of thresholds, are tomogram artifacts, particle movement, and limitations in signal/noise.

Table 3 Volume fractions of phases segmented from the entire masked volume of the sequence of registered tomograms of mini-plug 7_C. Solid mineral phase fractions and porosities are given as percentage of total bulk volume (BV), and liquid saturations as percentages of total pore volume (PV).

	Grain (%BV)	Clay (%BV)	Macro-porosity (%BV)				Micro-porosity (%BV)		Total Porosity (%BV)	
Dry	76.7	2.2	17.2				3.9		21.1	
			Oil (%PV)		Brine (%PV)		Oil (%PV)	Brine (%PV)	Oil (%PV)	Brine (%PV)
SIH			57.8		23.5		2.8	15.8	60.6	39.3
SIL			54.1		27.1		3.2	15.5	57.3	42.6
			OO (%PV)	BO (%PV)	OB (%PV)	BB (%PV)				
SIL/SIH difference			53.3	1.2	4.5	22.3				

1D profiles of residual oil volume, either longitudinally down the mini-plug (in which each tomogram cross-sectional slice is averaged) or radially (See Supplementary material) serve to characterize any mini-plug-scale variations. The longitudinal profile of the volume fraction of each segmented phase in the SIH state is plotted against height from top to bottom of the field of view of mini-plug 7_C in Figure 9(a). Macro- and micro-porosity have uniform profiles, indicating that this outcrop rock is homogenous over these scales. As expected, macro-porosity exhibits larger amplitude variations than micro-porosity. These same variations are mirrored in the profile of macro-oil, as it mainly resides in larger pores, while macro-brine resides in smaller resolved pores or the corners of larger ones, and thus exhibits a flatter profile, similar to that of micro-brine.

Longitudinal profiles of total oil volume fraction (summing macro- and micro-oil) after SIH and SIL, as well as OB, BO and oil change (the difference OB minus BO) are given in Figure 9(b). The total oil profiles, which can now be seen on this expanded vertical scale to rise slightly from mini-plug top to bottom, exhibit the same local variations in SIH and SIL. These peaks and troughs cancel out in the profile of oil change to yield a much flatter profile, reflecting the fact that most salinity-induced changes involve only a slight pore-scale rearrangement or movement of menisci. The weak trend to rising oil saturation towards the bottom coincides with a similar rise in porosity there. The oil change profile shows that the low salinity effect appears to exhibits a slight peak towards the middle of the mini-plug, and dips quite noticeably very close to the

bottom of the field of view due to a rise in BO from its typically very low levels. As the bottom of the tomogram field of view is about 3 mm above the bottom of the mini-plug, it is likely that this rise in BO and dip in oil change are artifacts resulting from a slight non-uniformity in tomogram grayscale arising near the end of the acquisition.

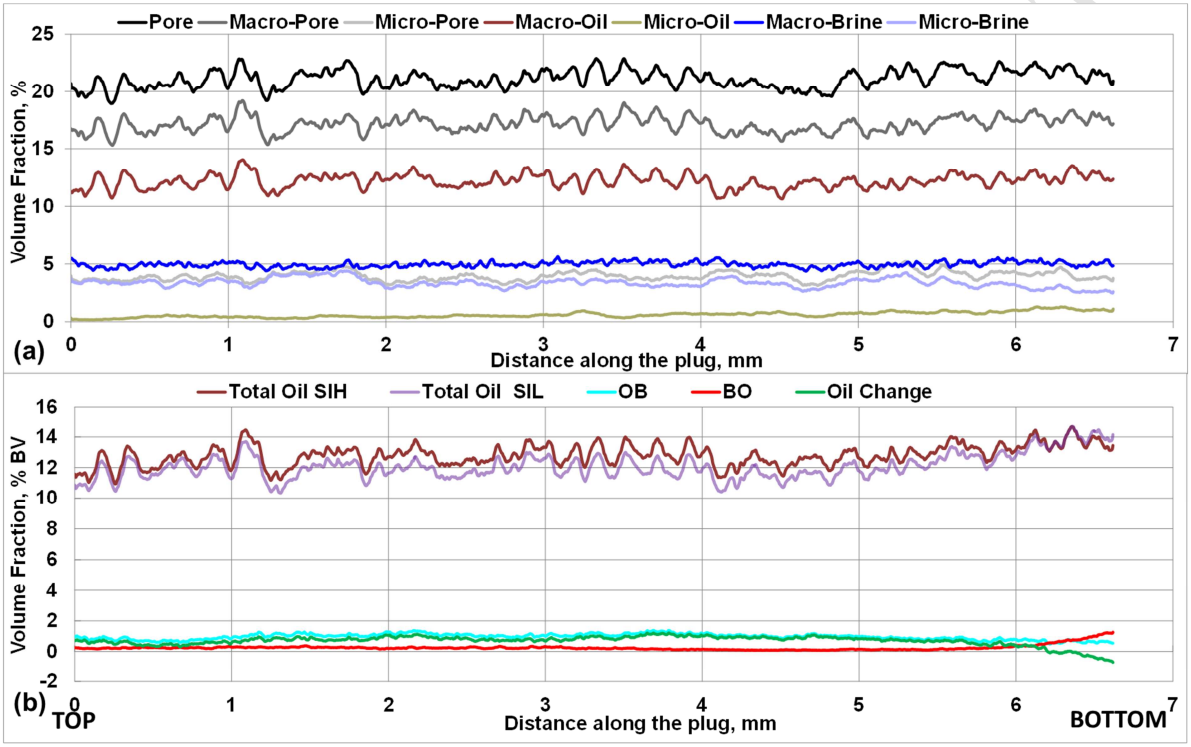

Figure 9. (a) Longitudinal profiles of volume fraction, as percentage of total bulk volume (BV), of all segmented phases of mini-plug 7_C in its SIH state, and (b) comparison of oil volume fractions and changes from SIH to SIL.

3.4 Pore-scale Distribution and Connectivity of Residual Oil

Having dealt with overall residual oil saturation and its mini-plug-scale distribution, the next step is analysis of the pore-scale distribution to get closer to the underlying mechanisms of oil recovery during SIL. For this purpose, the segmented macro-pore space was partitioned into labeled individual pore bodies using a watershed algorithm (Sheppard et al., 2014), onto which the segmented macro-oil after SIH and SIL was overlain to directly compare the oil saturation per pore. This results in the scatter plot of residual macro-oil saturation after SIH and SIL versus

the volume of each individual pore as given in Figure 10(a-b). A moving average is also plotted to clarify the overall trend versus pore size, along with the corresponding volume-weighted distribution curve to show the contribution to overall residual oil saturation.

The tomogram images shown and discussed above demonstrated that the smallest resolved pores have high brine saturation, and that sub-resolution porosity extends this trend to even higher brine saturations. The upward trend in residual oil saturation towards the left end in Figure 10(a-b) is thus thought to be an artifact from the partitioning of these extremely small voxelated pores. The moving average increases as expected over pore volumes large enough to contribute significantly to overall saturation, although with considerable scatter around it; pores of size around 10^{-3} mm^3 commonly exhibit oil saturations ranging from 60 to 90%, and instances of much lower saturation are still common. The impression from Figure 10(a-b) is that the moving average is shifted downwards from SIH to SIL fairly uniformly over all pore sizes, while the decrease in the cumulative distribution is naturally skewed toward larger pores.

Greater insight into the effect of salinity can be obtained from the corresponding plot of the oil change ($S_{O(SIH)} - S_{O(SIL)}$) per individual pore, which is given in Figure 10(c). Based on the moving average, the low salinity effect exhibits a slight peak at pore volumes just below 10^{-3} mm^3. This also corresponds to the sizes over which the scatter is greatest, mainly in OB (oil displacement by brine) but also in the slight counter-effect of BO (moved oil subsequently displacing brine). While the contribution of pores of this intermediate size to overall residual saturation in Figure 10(a-b) is much less than from larger pores, they provide the clearest hallmark of the slight shift toward a more water-wet state.

Connectivity was calculated by the GangliaCount algorithm (Kumar et al. 2010, Singh et al. 2011), which tracks the number of adjoining pore bodies that each connected oil blob spans and occupies a substantial fraction of (with this oil saturation cut-off value taken here as 50%). The resulting volume-weighted distribution curves, normalized to 100% of the residual oil volume, are shown in Figure 10(d), in which a blob occupying 1 or 2 pores is a singlet or a doublet, and so on. After SIH, 60% of the residual oil volume remains connected throughout the masked tomogram as one giant cluster. The upward and leftward shift from SIH to SIL clearly demonstrates that oil is less connected after tertiary recovery. The frequency of smaller blobs is increased in SIL, and the largest blob now only comprises 20% of all oil volume. Oil

connectivity thus provides a more sensitive indicator than oil saturation of the significant shift towards a water-wet state due to blob retraction and snap-off.

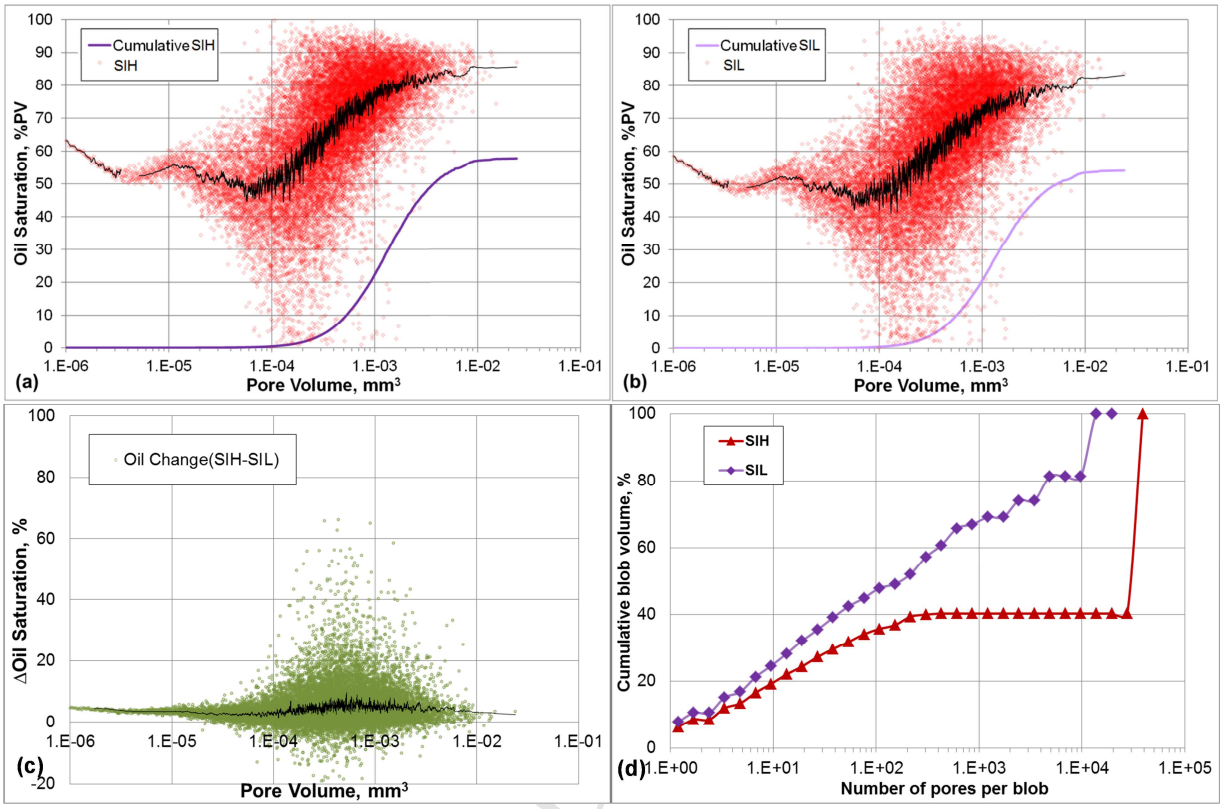

Figure 10. Scatter plot of residual oil saturation in each resolved pore body versus its individual volume (red points), also showing moving average (black line) and volume-weighted cumulative distribution (purple curve) after (a) SIH followed by (b) SIL, in mini-plug 7_C. (c) Scatter plot of change in residual oil saturation (SIH minus SIL) in each resolved pore body versus its individual volume. (d) Cumulative distribution of residual oil volume after SIH and SIL, as a function of the number of connected pores spanned by each separate ganglion

3.5 Interfacial Areas of Residual Oil

The resolved residual oil shares interfaces with brine, with grains and with external surfaces of clay aggregates. Area was calculated using an algorithm for smoothing of voxelated interfaces, and the average values over the masked tomogram are shown in Figure 11(a-d). Figure 11(a) shows the percentage breakdown of total area in the system into its contributions from all six possible interfaces between the four resolved, segmented phases. Oil recovery from SIH to SIL

reduces the oil contact with grains (with a concomitant gain in brine-grain area) and increases the oil-brine interfacial area. Figure 11(b) shows that grains offer more surface area than external clay surfaces (at tomogram resolution, with smoothened voxels), and grains more commonly contact oil than brine while clays more commonly contact brine than oil. Figure 11(c) shows that i) the decrease in oil contact area from SIH to SIL is greater for grain than clay when counted per total pore wall area (/Pore-rock), and that ii) this tendency becomes stronger when the count is more correctly weighted by the available area presented by grain or clay (/Pore-mineral), and that iii) this tendency becomes even stronger when the count is even more correctly weighted by the starting area of oil contacting grain or clay in the SIH state (/Oil-mineral). Figure 11(d) shows that oil-brine interfacial area is roughly one-quarter of pore wall area, and its increase from SIH to SIL is, as expected, primarily due to interfaces created by brine displacing oil (OB) rather than by oil re-displacing brine (BO). The conclusion consistently supported by these various measures is that tertiary recovery by low salinity brine in this case is due to preferential detachment of oil from grains, not clay external surfaces.

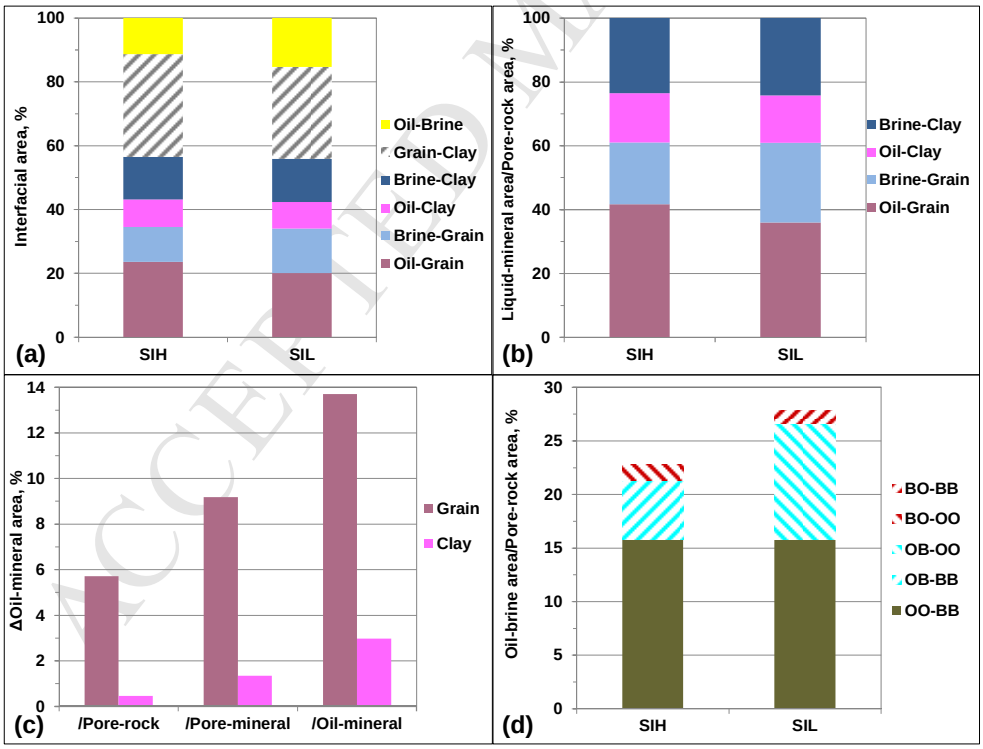

Figure 11 (a) Overall statistics of interfacial area for each resolved phase combination after SIH and SIL, normalized to 100%, (b) Interfacial area of each (resolved) liquid (oil or brine) with grain or clay, relative to total pore-rock area, (c) salinity-induced change in interfacial area of oil with grain or clay, normalized

in three ways, and (d) oil-brine interfacial area, relative to total pore-rock area, for mini-plug 7_C. Here rock refers to grain plus clay, while mineral refers to grain or clay.

3.6 Oil/Brine Interfacial Mean Curvature

Calculation of the local mean curvature of the oil-brine interface provides further insight into wettability changes from SIH to SIL. From the Young-Laplace equation, capillary pressure is directly proportional to mean curvature, which in turn is dictated by the pore geometry and the contact angle. A subset of 1000 × 887 × 1800 voxel^3 was selected in the middle of the mini-plug 7_C tomograms, within which the area-weighed mean curvature of the resolved, segmented oil-brine interface was obtained using a Monge geometrical algorithm (Wildenschild and Sheppard 2013). The average mean curvature and area of each of four categories of moving interfaces, i.e. OB, BO, BB and OO, are listed in Table 4. Interfaces OB-BB are those in SIH which moved due to brine advance to form an OB-OO interface in the SIL state. The mean curvature of these switches from negative in SIH to positive in SIL in Table 4. This local increase in oil-brine meniscus curvature implies a decrease in the water-advancing contact angle, and thus a shift toward more water-wet. Interfaces BO-OO are those in SIH which moved due to oil re-advance (secondary water-receding) to form a BO-BB interface in the SIL state. The mean curvature of these switches from positive in SIH to negative in SIL in Table 4. This local decrease implies an increase in secondary water-receding angle. However, owing to the very small volume of BO relative to OB, as reflected in their corresponding areas in Table 4, the contribution of water-advancing interfaces to the system is much higher than the slight counter-effect from water-receding interfaces.

Table 4 Average mean curvature, H, and total area of the four pore-occupancy categories segmented between SIH and SIL in mini-plug 7_C.

State	Interface category	H (μm^{-1})	Area (mm^2)
SIH	OB-BB	-0.035	30.3
SIL	OB-OO	0.046	52.8
SIH	BO-OO	0.021	2.4
SIL	BO-BB	-0.199	3.2

To visualize oil blob movement from SIH to SIL, two representative examples of iso-surfaces were generated and are given in Figure 12(a-b). The first example in Figure 12(a) shows oil in SIH which fills a pore body and covers most of its walls, and which is connected through one throat at left. During SIL, the blob detaches from the walls and retracts by local advance of low salinity brine. The shrinkage of the oil ganglion end is associated with increase in mean curvature of this OB interface in SIL, in line with the trend in Table 4. The second example in Figure 12(b) shows two snap-off events in which a large oil ganglion that is internally connected via two throats in SIH breaks into smaller, more disconnected oil blobs after SIL. The snap-off appears to be driven by detachment of oil from the pore body walls and subsequent thickening of these films of low salinity brine to destabilize the oil configuration in the throats. Again the more rounded OB interfaces enclosing oil in SIL lead to an increase in mean curvature, due to the rock grains becoming more water-wet.

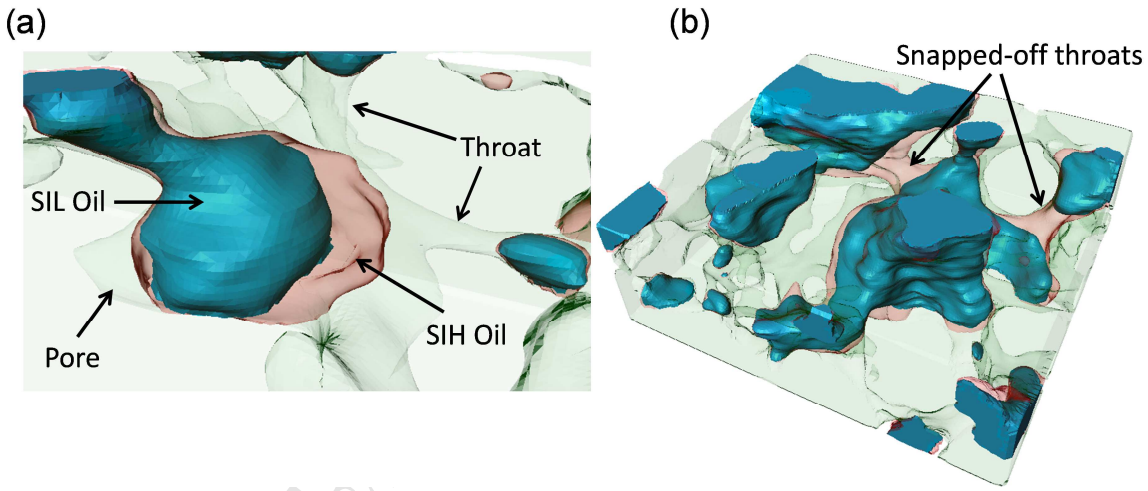

Figure 12 Iso-surfaces of oil blobs after SIH (brown) and SIL (green), showing (a) close-up of an oil ganglion detaching and receding in a single pore (0.26 × 0.16 × 0.10 mm), and (b) changes in oil distribution and connectivity, featuring snap-off events, over a larger sub-volume (0.50 × 0.46 × 0.16 mm).

4. Conclusion

Micro CT 3D imaging and analysis is a robust tool for studying multiphase fluid distributions within porous materials. A previous study (Zhang and Morrow 2006) of the low salinity effect in

water flooding of Berea sandstone plugs, which showed fairly weak and variable responses, was mimicked here using mini-plugs subjected to immersion in sequences of these same high and low salinity brines for micro-CT imaging and analysis of recovery of the same crude oil by spontaneous imbibition. The imaged experiments also showed a fairly weak and variable low-salinity effect. Fines movement during SIH and SIL was occasionally seen, and sometimes appeared to stem from loosely-bound coring debris. This demonstrated that pore-scale mobilization of clays by the oil-brine interface, at sufficiently low level as to not cause throat blocking and formation damage, can occur and contribute to the low salinity effect. However, most oil displacement did not appear (at tomogram resolution) to coincide with such fines movement. A mini-plug with additional recovery of 3.0% OOIP by low salinity in tertiary mode was selected for further image analysis. A methodology was developed to take advantage of acquisition and registration of a sequence of imaged states of this mini-plug to quantitatively segment oil and brine in resolved and sub-resolution pores. All metrics pointed to a slight shift towards a more water-wet state, mainly driven by oil in larger pores being preferentially detached from grain surfaces rather than from internal or external surfaces of pore-filling clay aggregates (primarily kaolinite). The results could imply that oil release from clays is not the main mechanism of the low salinity effect; conversely though, it could be argued that the small effect seen here for Berea sandstone was due to be absence of this primary cause.

Acknowledgements

Financial support from the member companies of the Digital Core Consortium Wettability Satellite and Statoil are acknowledged.

Abbreviations

Micro-CT: X-ray micro-tomography

SI: Spontaneous imbibition

SIH: spontaneous imbibition of high salinity brine

SIL: spontaneous imbibition of low salinity brine

SILL: very low salinity brine

SEM: scanning electron microscopy

SEM-EDS: energy dispersive x-ray spectroscopy

MRB: Minnelusa reservoir brine

OOIP: original oil in place

MICP: Mercury injection capillary pressure

$S_{or:}$ residual oil saturation

$S_{oi:}$ initial oil saturation

S_{wi}: initial water saturation

PV: pore volume

BV: bulk volume

BB: brine-filled in SIH and SIL

OO: oil-filled in SIH and SIL

OB: oil-filled in SIH but brine-filled in SIL

BO: brine-filled in SIH but oil-filled in SIL

$S_{O(SIH):}$ residual oil saturation at high salinity spontaneous imbibition state

$S_{O(SIL):}$ residual oil saturation at low salinity spontaneous imbibition state

5. References

1. Morrow, N. R., Buckley, 2011, Improved oil recovery by low-salinity waterflooding, J. Pet. Tech., 63, 106-110.

2. Masalmeh, S. et al. 2014. Low-Salinity Flooding: Experimental Evaluation and Numerical Interpretation, IPTC-17558-MS.

3. G.Q. Tang, N.R. Morrow, 1999, Influence of brine composition and fines migration on crude oil/brine/rock interactions and oil recovery J. Pet. Sci. Eng., 24, pp. 99–111.

4. Aladasani, A. et al., 2012, Investigating low-salinity waterflooding recovery mechanisms in sandstone reservoirs, SPE 152997.

5. M. Cissokho, et al., 2010, Low salinity oil recovery on clayey sandstone: experimental study Petrophysics, 51, pp. 305–313.

6. McGuire, P.L., Chatham, Jr., 2005, Low Salinity Oil recovery: An Exciting New Opportunity for Alaska′s North Slope, Paper SPE 93903.

7. Lager, A., et al., 2006, Low salinity oil Recovery – An Experimental Investigation, SCA -36.

8. Ligthelm, D.J. et al., 2009, Novel Waterflooding Strategy by Manipulation of Injection Brine Composition, SPE 119835.

9. Sandengen, K., Arntzen, O.J., 2013, Osmosis During Low Salinity Water Flooding. Paper A-19 presented at the 17th European Symposium on Improved Oil Recovery. St. Petersburg, Russia.

10. Wang, X.C., Lee, C., 1993. Adsorption and desorption of aliphatic amines, amino acids and acetate by clay minerals and marine sediments, Marine Chem, 44, pp. 1-23.

11. Parfitt, R.; Greenland, D., 1970, The adsorption of poly(ethylene glycols) on clay minerals, Clay Miner, 8, pp. 305-315.

12. Yasaman Assefa et al., 2014, Application of nanofluid to control fines migration to improve the performance of low salinity water flooding and alkaline flooding, JPSE, Volume 124, Pages 331–340.

13. Berg, S. et al., 2010, Direct experimental evidence of wettability modification by low salinity, Petrophysics, 51, pp. 314–322.

14. Cense, A.W et al. 2011, Direct visualization of designer water flooding in model experiments, SPE 144936.

15. Rivet, S.M et al., 2010, A coreflood investigation of low-salinity enhanced oil recovery, SPE 134297.

16. Sorop, T.G.,et al., 2013, Integrated approach in deploying low salinity waterflooding, SPE 165277.

17. Zhang, Y., Morrow, N.R., 2006, Comparison of Secondary and Tertiary Recovery With Change in Injection Brine Composition for Crude Oil/Sandstone Combinations, SPE 99757.

18. Kumar, M. et al. 2010. Visualizing andQuantifying the Residual Phase Distribution in Core Material.Petrophysics 51 (5): 323-332.

19. K. Singh et al. 2011, Remobilization of residual non-aqueous phase liquid in porous media by freeze-thaw cycles, Environmental Science & Technology 45(8):3473–3478.

20. D Wildenschild, AP Sheppard, 2013, X-ray imaging and analysis techniques for quantifying pore-scale structure and processes in subsurface porous medium systems, Advances in Water Resources 51, 217-246.

21. Shabaninejad M. et al., 2015, Micro-CT Pore-scale Analysis of Low Salinity Recovery from Reservoir Sandstones, 77th EAGE Conference and Exhibition 2015

22. Shabaninejad M. et al., 2017, Pore-scale analysis of residual oil in a reservoir sandstone and its dependence on water flood salinity, oil composition and local mineralogy , energy and fuel.

23.W.B. Bartels et al., 2017, Fast X-ray micro-CT study of the impact of brine salinity on the pore-scale fluid distribution during waterflooding,Petrophysics, 58 (1), pp. 36-47.

24. Alireza Emadi, Mehran Sohrabi, 2012, Visual Investigation of Low Salinity Water Flooding, International Symposium of the Society of Core Analysts held in Aberdeen, Scotland, UK.

25. Sheppard, A.P et al, 2004, Techniques for image enhancement and segmentation of tomographic images of porous materials. Physica a-Statistical Mechanics and Its Applications, 339: p. 145-151.

26. Qianhao Cheng, 2015, Application of Contrast Techniques in X-ray Microtomography to Characterization of Rocks and Hydrocarbon Recovery, Master of philosophy thesis, The Australian National University.

27. Sheppard, A.P et al, 2014, Techniques in helical scanning, dynamic imaging and image segmentation for improved quantitative analysis with X-ray micro-CT Nuclear Instruments and Methods in Physics Research: Section B 324, 49-56.

Highlights

- A methodology was developed to quantitatively segment oil and brine in resolved and sub-resolution pores
- All metrics pointed to a slight shift towards a more water-wet state after low salinity brine
- Oil in larger pores being preferentially detached from grain surfaces rather than from internal or external surfaces of pore-filling clay